Journal of Alloys and Compounds 927 (2022) 167077

Contents lists available at ScienceDirect

Journal of Alloys and Compounds

journal homepage: www.elsevier.com/locate/jalcom

Ameliorating the electrode/electrolyte interface compatibility in Li-ion solid-state batteries with plasticizer

Jae-chang Seol[a], Ramkumar Balasubramaniam[a], Vanchiappan Aravindan[b,*], Ranjith Thangavel[c], Yun-Sung Lee[a,*]

[a] Faculty of Chemical Engineering, Chonnam National University, Gwangju 500757, South Korea
[b] Department of Chemistry, Indian Institute of Science Education and Research (IISER), Tirupati 517507, India
[c] School of Energy Science and Engineering, Indian Institute of Technology Guwahati, Guwahati 781039, India

ARTICLE INFO

Article history:
Received 2 March 2022
Received in revised form 11 August 2022
Accepted 1 September 2022
Available online 3 September 2022

Keywords:
Composite solid electrolytes
Plasticizer
Lithium ionic conductivity
Solid-state battery
Homogeneous distribution
Solution casting method

ABSTRACT

Composite solid electrolytes (CSEs) based on poly (vinylidene fluoride-co-hexafluoropropylene) (PVDF-HFP)/LiTFSI/LLZO/different wt% of tetra-ethylene-glycol-dimethyl-ether (TEGDME) were prepared using the facile solution casting method or phase-inversion method. X-ray diffraction (XRD) and Fourier transform infrared (FTIR) spectroscopy measurements were used to identify the structures and complexations of the prepared electrolyte films. The morphology and thermal stability of the electrolytes were investigated using field-emission scanning electron microscopy (FE-SEM) and thermogravimetric analysis (TGA). The ionic conductivity of all electrolyte films was analyzed using AC impedance analysis between 298 and 353 K. The data supports that the 30 wt% TEGDME CSE exhibited the highest ionic conductivity (6.2×10^{-5} S cm^{-1} at 25 °C and 3.6×10^{-4} S cm^{-1} at 60 °C) and a wide electrochemical window (4.87 V *vs.* Li/Li$^+$). A solid-state battery with $LiFePO_4$/Li-metal was cycled using the 0.1 C rate at 60 °C for 100 cycles, resulting in a high initial discharge capacity of 157 mAh g^{-1} with a good coulombic efficiency of > 99%. This admirable electrochemical performance can be attributed to the high ionic conductivity of the electrolyte and its electrochemical stability. We emphasize the significant role of the TEGDME plasticizer in the performance of the CSE as well as the ionic conductivity and compatibility of the electrolyte with the electrode in the solid-state battery. All encouraging results confirm that the CSE has the potential to be a high-voltage electrolyte for Li-ion solid-state batteries.

1. Introduction

Secondary lithium-ion batteries (LIBs) have attracted considerable attention as energy storage devices in the portable device market and for electric vehicles because of their relatively high energy density, long life cycle, high output voltage, and low self-discharge rate [1–4]. Such safe and reliable batteries are a necessity for the charge/discharge process in hybrid electric vehicles. Flammable solvents, limited power capability, and Li-dendrite formation due to irregular metallic Li deposition during repeated charge/discharge processes restrict the future applications of Li-ion batteries [1,5]. Solid-state electrolytes (SSE) are emerging as the most promising options for LIBs because of their wide electrochemical window, thermal stability, and safety [6,7]. Moreover, their mechanical strength hinders Li-dendrite formation, thereby reducing the safety hazards of all-solid-state Li-ion batteries (ASSLIB) [8,9].

Therefore, solid electrolytes (SEs) are considered to be an optimal candidate for replacing liquid electrolytes in LIBs. In general, SEs are categorized into (i) ceramic electrolytes and (ii) organic polymer electrolytes. Inorganic ceramic electrolytes can be classified based on system type, such as perovskite-type ($Li_{3x}La_{2/3-x}TiO_3$, LLTO), NASICON-type $LiM_xZ_{2-x}(PO_4)_3$, M=Al, Z = Ti, Ge), garnet-type ($Li_7La_3Zr_2O_{12}$), and sulfide-type system (Li_2S–Al_2S_3–GeS–P_2S_5) and its derivatives [5,10–13]. Compared with polymer electrolytes, ceramic SSEs afford high ionic conductivity, excellent thermal stability, and high Li-ion transfer numbers (t_{Li+}~1) [14,15]. Nevertheless, their brittle nature and high interfacial resistance, which is attributed to poor mechanical contact with the electrodes, restrict the usage of oxide SEs [16,17]. The narrow window of electrochemical stability due to oxidative decomposition at a relatively low voltage, such as for $Li_{10}GeP_2S_{12}$ (LGPS) at 2.15 V and for Li_3PS_4 (LPS) at 2.41 V *vs.* Li/Li$^+$ and its inherent chemical potential incompatibility with a

* Corresponding authors.
E-mail addresses: aravind_van@yahcoo.com (V. Aravindan), leeys@chonnam.ac.kr (Y.-S. Lee).

https://doi.org/10.1016/j.jallcom.2022.167077
0925-8388/

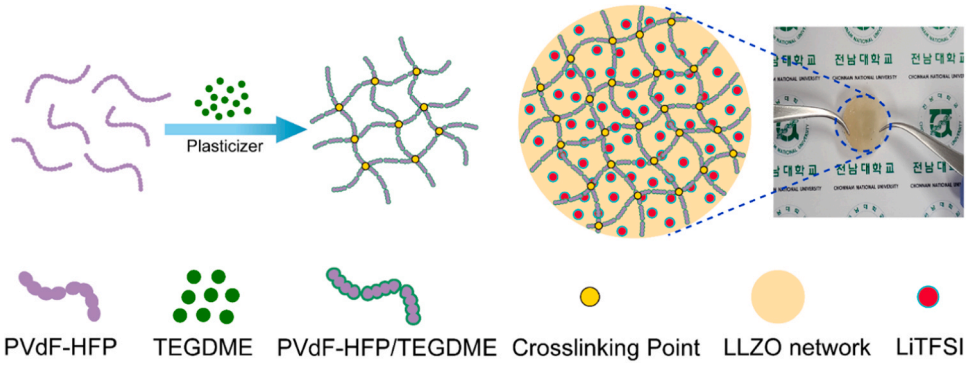

Fig. 1. Schematic diagram of preparation of composite solid electrolytes (CSE0–40).

Li-metal anode, restricts the usage of sulfide electrolytes [16]. Especially solid polymer electrolytes (SPEs) with polymer matrices, such as polyethylene oxide (PEO), polyacrylonitrile (PAN), polymethyl methacrylate (PMMA), and polyvinylidene fluoride (PVDF), have attracted much attention due to their excellent flexibility and easy preparation [16,18,19]. The low ionic conductivity, poor mechanical strength and high interfacial impedance with electrodes at 25 °C are the shortcomings of polymer-based electrolytes and inhibit practical applications in LIBs [20]. The preparation of safe and reliable electrolytes is still challenging.

Compared with other polymer electrolytes, poly(vinylidene fluoride-hexafluoropropylene) (PVDF-HFP) has a high dielectric constant (ε = 8.4), which facilitates a high concentration of charge carriers. It also has both an amorphous (-HFP) and a crystalline phase (-VDF) [21,22]. The amorphous phase of PVDF-HFP facilitates fast ion transfer, and the crystalline phase increases the mechanical strength of the electrolyte [22]. The ion transfer path mostly depends on the amorphous region as the crystalline phase does not favor Li-ion transport [19]. Overcoming the obstacles of incorporating a ceramic filler (*e.g.*, Al_2O_3, ZrO_2, SiO_2, and TiO_2) into the polymer matrix can increase the disorder region in order to increase the ionic conductivity [19,23,24]. However, these ceramic fillers are electrochemically inactive, and excessive use of filler decreases the ionic conductivity and increases the mass of the battery. Particularly, a Li-ion ceramic filler (LLZO) is an optimal candidate due to its high ionic conductivity (10^{-4} to 10^{-3} S cm^{-1}) and good compatibility with the Li-metal anode [25,26]. As a promising strategy, composite solid electrolytes (CSEs) have captured the attention of many researchers because of the synergetic combination of ion-conducting polymers and Li-ion ceramic fillers. CSEs have also been attracting attention due to their promising features for innovative real-world applications in flexible and safe energy storage devices.

However, CSEs with Li-ion ceramic fillers still suffer from relatively low ionic conductivities. Adding the plasticizer is an effective way to enhance the ionic conductivity of the CSE. Recently, many reports have been made on the improvement of ionic conductivity of the PVDF-HFP-based polymer electrolytes with plasticizers; for example, Ulaganathan et al. [26] studied the surface morphologies and conductivity of PVDF-HFP/PEMA electrolytes prepared with different wt% of Li-salts and plasticizer, propylene carbonate (PC). Wei et al. [27] and Yang et al. [28] investigated the Li/$LiFePO_4$ and Li/NCM811 battery cells, respectively, using an appropriate Succinonitrile (SN) plasticizer. [27,28] But the PC is flammable, and SN is reactive with Li-metal. [29] Herein, we were using a tetra-ethylene-glycol-dimethyl-ether (TEGDME) as a plasticizer for the preparation of CSE. More importantly, the TEGDME is a non-flammable solvent and has good stability with Li metal anode is worth mentioning. [30] The TEGDME solvent assists in increasing the free volume of the polymer as well as lowering the glass transition temperature of the polymer [18]. Furthermore, the incorporation of TEGDME plasticizers enhances the ionic conductivity, the compatibility of the CSEs with the electrode, and the release of mobile charge carriers due to the ion-dissolution effect [27]. In this work, we prepared a CSE based on PVDF-HFP and an LLZO ceramic filler using a simple solution casting method or phase-inversion method. The prepared CSEs revealed high ionic conductivity (1.13×10^{-4} S cm^{-1} at 25 °C and 3.01×10^{-4} S cm^{-1} at 60 °C), a good electrochemical window (4.76 V *vs.* Li/Li^+), decent thermal stability, and low interfacial resistance. The symmetric cell shows an excellent life cycle with the Li-metal anode, and the expectations of CSE are high for use in next-generation energy storage devices. A solid-state battery based on a $LiFePO_4$ cathode, PVDF-HFP (LiTFSI) - LLZO – 30% TEGDME, and a Li-metal anode shows a high capacity at a 0.1 C rate for 100 cycles.

2. Experimental section

2.1. Preparation of composite solid electrolyte

PVDF-HFP (LiTFSI) – LLZO – with different wt% of TEGDME solid electrolyte was prepared using facile solution casting or the phase-inversion method. Initially, LiTFSI (30 wt%) - TEGDME (different CSE0, CSE10, CSE20, CSE30, and CSE40 wt%) were dissolved in N, N-dimethylformamide (DMF) and different wt% concentrations of PVDF-HFP (70, 60, 50, 40, 30 of the total wt%), and an excess of 10 wt % of LLZO nanoparticles (Jeong Kwan Co. Ltd. Korea) were added to the solution. The as-prepared solution was stirred continuously for uniform dispersion of the nanoparticles in the PVDF-HFP polymer matrix. The resulting homogeneous solution was cast onto the surface of a Mylar sheet using a glass rod. The prepared CSE was dried at 80 °C for 12 h under a vacuum to remove any residual solvent in the electrolyte. The dried electrolyte was punched into the appropriate size (diameter = 1.8 cm) and immediately transferred to a glovebox for further electrochemical studies (Fig. 1).

The composite cathode slurry was prepared by mixing $LiFePO_4$ (MTI Co. Ltd.) active material, a CSE, Super P, and PVDF (weight ratio of 50:20:20:10) in an NMP solution. The slurry was cast onto an aluminum foil and then dried at 120 °C for 12 h under a vacuum. The electrode was cut into pieces (size = 1.4 cm) and transferred to the glovebox for assembly of the cell under an argon atmosphere. The mass of the electrode was in the range of 1–1.3 mg cm^{-2}. Li-metal foil was used as the anode and PVDF-HFP-30 wt% TEGDME-10 wt% LLZO was used as the separator. The LFP/Li cell was charged and discharged at a 0.1 C rate at 60 °C in the potential range of 2.8–4.0 V. For comparison, and the LFP liquid cell was assembled using 1 M $LiPF_6$ (EC/DMC 1:1 in v/v) electrolyte. The cathode was prepared using $LiFePO_4$:ketjen black: teflonized acetylene black (TAB) according to our previously reported work in the weight ratio of 7:1.5:1.5 [3,28].

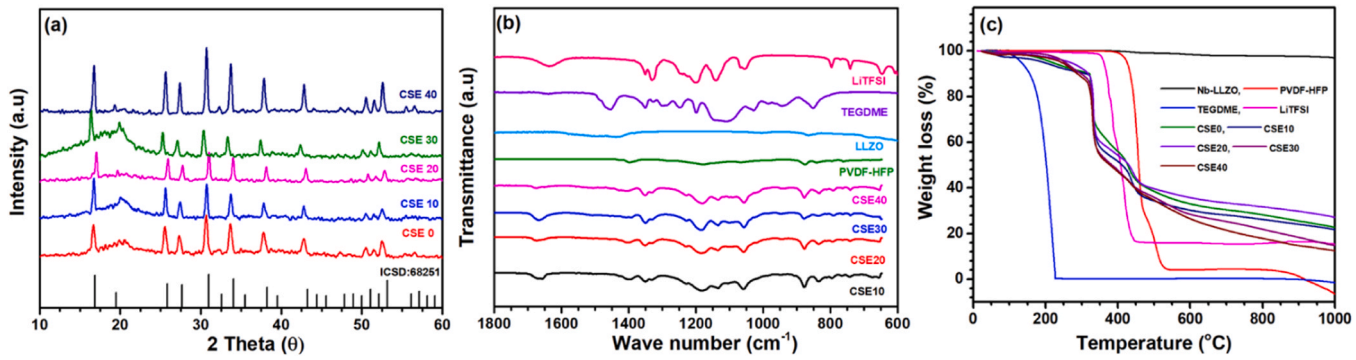

Fig. 2. (a) XRD patterns of CSE0-40 electrolytes, (b) FTIR analysis of LiTFSI salt, TEGDME plasticizer, LLZO ceramic filler, PVDF-HFP polymer, and CSE0–40 electrolytes and (c) TGA curves of CSE0–40, LLZO, PVdF-HFP, TEGDME, and LiTFSI.

2.2. Sample characterizations

Crystal structures of the LLZO powder and the CSEs were examined using a high-resolution X-ray diffractometer (HR-XRD, Rigaku, Japan, D/MAX Ultima III). The surface morphology, chemical structure, and elemental distribution of the LLZO powder and CSEs were studied using a field-emission scanning electron microscope (FE-SEM/EDX Hitachi, Japan, S-4700/EX-200). Thermal analysis of the CSE was carried out using thermogravimetric analysis (TGA/DSC, Shimadzu, Japan, TGA-50/DSC-60) in the temperature range of 25–800 °C under an argon atmosphere with an increased rate of 5 °C min^{-1}. The molecular functional group analysis was performed by Fourier transform infrared spectroscopy (FT-IR, Shimadzu, Japan, IRPresitge-21) in the wavelength range of 4000–400 cm^{-1}. X-ray photoelectron spectroscopy (XPS) was performed using study the surface elemental analysis of the electrolyte and cathode materials.

2.3. Electrochemical studies

The electrochemical impedance spectra of the CSEs were recorded using an electrochemical workstation (Biologic, model VSP France) in the temperature range of 25–80 °C and for frequency between 100 kHz and 0.01 Hz with an applied potential of 10 mV. The cell setup for the impedance measurement contained an electrolyte sandwiched between two stainless steel blocking electrodes (diameter is 1.6 cm). The linear sweep voltammetry (LSV) of the CSEs was studied using an asymmetric cell (Li/CSE/SS) at a scan rate of 1 mV s^{-1} in the potential range 0–5 V (Biologic, Model VSP France). An analysis of the Galvanostatic charge-discharge performance of the symmetric cell (Li/CSE/Li) was carried out using an electrochemical analyzer (Biologic, model VSP France) with a cell working current density of 0.1 mA cm^{-2}. The charge-discharge performance of the LFP/CSE/Li cell was studied in the potential range of 2.8–4 V with a current density of 0.1 C rate at 60 °C using an Arbin BT-2000 battery test system.

3. Physical characterization

3.1. X-ray diffraction analysis

Fig. 2a shows the XRD patterns of LLZO, CSE0, CSE10, CSE20, CSE30, and CSE40 composite solid electrolytes. The characteristic diffraction peaks of CSE0–40 match well with those of the cubic-phase garnet parent $Li_5La_3Nb_2O_{12}$ structure (ICSD collection code: 68251) [5,12,29]. This demonstrates that after physical mixing, the cubic phase is preserved in CSE0–40 and that there are no impurities in CSEs. The LiTFSI salt characteristic peaks were absent in CSEs, which is attributed to the complete dissolution of the salt in the polymer matrix, which indicates that the salt is not present in an isolated phase. The amorphous nature of the electrolyte was confirmed by the broad humps in the XRD pattern. The presence of the plasticizer (TEGDME) in the CSE increased the amorphous region, and consequently, promotes the free Li-ion movement easily in the electrolyte. For comparison we were provided XRD pattern of films based on pure PVDF-HFP with different wt% of TEGDME plasticizer (Fig. S1). Therefore, the ionic conductivity of the CSE was considerably increased. Furthermore, the added LLZO strengthened the polymer and provided ion transfer paths for Li-ions, which significantly enhanced the migration of ions [27,30].

3.2. FT-IR analysis

FTIR is an important tool for understanding the complex developments in terms of molecular and structural changes between the polymer, Li-salt, ceramic fillers, and plasticizers. Fig. 2b represents the FTIR spectra of PVDF-HFP, the LiTFSI salt, the LLZO ceramic filler, and the TEGDME plasticizer. In pure PVDF-HFP, the peaks at 1396, 1278, 1178, 1068, 975, 875, 840, 794, and 761 cm^{-1} correspond to -CH_2 wagging, -CF_3 symmetric stretching, -C-C-C- symmetric bond stretching, C-F symmetric stretching vibrations, C-F stretching vibrations, combined -C-C-, and CF_2 symmetric stretching vibrations, mixed CH_2 rocking modes, CF_3 stretching vibrations, and CH_2 rocking vibrations, respectively [22,31,32]. For pure LiTFSI salt peaks were observed at 1631, 1350, 1201, 1109, 1055, 607, and 514–574 cm^{-1} and correspond to SO_2 asymmetric stretching, the CF_3 symmetric stretching mode, C-F stretching, and C-CO_2-N bonding, the S-N-S symmetric stretching mode, the S-N symmetric stretching mode, the deformation mode of SO_2, and the CF_3 asymmetric bending mode, respectively [31,33,34]. Comparing the data of PVDF-HFP before and after incorporation of the Li-salt, the ceramic filler, and the plasticizer, it can be seen that the -CH_2 wagging peak shifted to 790 cm^{-1}, the combined -C-C- and CF_2 stretching vibrations shifted to 879 cm^{-1}, the mixed CH_2 rocking modes shifted to 837 cm^{-1}, and the CF_3 stretching vibration shifted to 790 cm^{-1}. The peak at around 1100 cm^{-1} corresponds to the C-O bonds representing the presence of TEGDME in CSE. Further, the PVDF-HFP characteristic peak intensity changed because of interactions between the polymer and LLZO, LiTFSI, TEGDME, and the organic solvent DMF [19]. The interactions between the plasticizer and polymer seen in the spectra of CSE are helpful for the ionic conductivity of the electrolyte.

3.3. Thermal analysis

The thermal stability of the electrolyte is a significant parameter for use in elevated temperature applications because it is related to the safety of the battery. In the present work, the electrolyte thermal stability was analyzed using thermogravimetric analysis (TGA) in the temperature range of 25–800 °C (Fig. 2c). Three different stages of

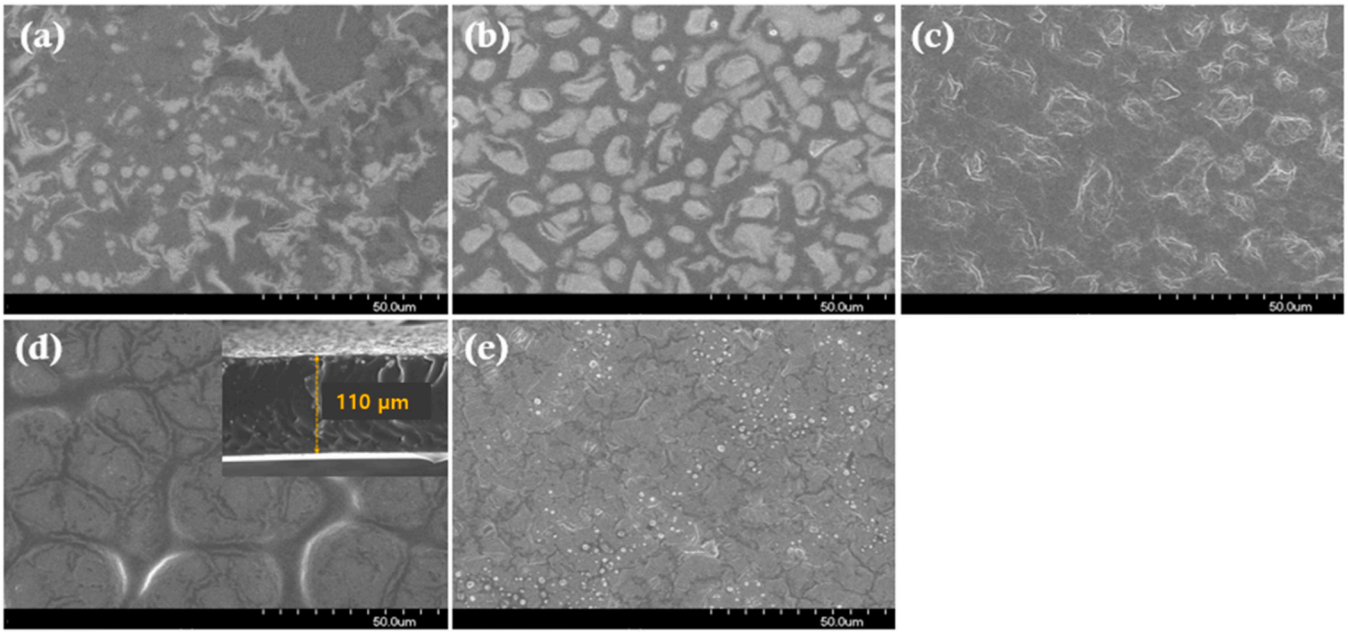

Fig. 3. Surface morphology of (a) CSE0, (b) CSE10, (c) CSE20, (d) CSE30, and (e) CSE40.

weight loss were observed for CSE. Below 130 °C, only negligible weight loss happened in the electrolyte. The first weight loss was observed in the temperature range of 150–300 °C as a result of TEGDME degradation, as the boiling point of TEGDME is 216 °C [35]. A steep weight loss slope in the graph denotes the partial decomposition of the LiTFSI salt in the matrix between 320 and 460 °C [36]. The last stage of the mass loss corresponds to PVDF-HFP polymer decomposition [37]. Above 540 °C, the CSE is maintained at 32.4% due to the introduction of the LLZO ceramic filler. This further confirms that LLZO improves the thermal stability of CSE.[7] Furthermore, we were checking the safety test of the CSE with lighting and heat at different temperatures. The flammability test was also carried out, and the results confirmed that the burning degree of CSE was low (Fig. S2). However, the thermal studies of CSE were also investigated at different temperatures in the range of 25–250 °C for 30 min (Fig. S3). The thermal test confirmed that the electrolyte is stable up to 100 °C; afterward, it melts and shrinks at 150 °C, then finally, it changes to black color at 200 °C.

3.4. Surface morphology analysis

Fig. 3a–e displays the surface morphology of PVDF-HFP/LiTFSI/10% LLZO with 0, 10, 20, 30, and 40 wt% of TEGDME respectively. The CSE membrane has a smooth surface and good compatibility with LLZO. Additionally, the thickness of the electrolytes was determined to be approximately around 110–120 µm. The optical image shows that the color of the PVDF-HFP/LiTFSI electrolyte and the CSE30 electrolyte is different (Figs. S4 and S5). The PVDF-HFP electrolyte is transparent without the addition of LLZO. After the incorporation of LLZO into the polymer matrix, the La atom in LLZO forms a complex with the N atom and the C═O group of the DMF solvent in addition to behaving like a Lewis base, which then leads to a change in the color to brown [19,38]. These images confirmed that the electrolyte membrane is flexible and that it is possible to cut it to the desired shape (Fig. S5). The energy-dispersive spectra (EDS) image confirmed that an LLZO ceramic filler existed in the polymer matrix. The elemental and cross-sectional images indicate that lanthanum, fluorine, and zirconium were homogeneously distributed in the polymer matrix (Fig. S6 a–d and S7). Polymer electrolyte EDS mapping confirms the presence and distribution of fluorine, nitrogen, carbon, and oxygen in the polymer matrix (Fig. S7).

4. Electrochemical performance of the composite solid electrolyte (CSE)

4.1. Ionic conductivity and electrochemical stability

Electrochemical impedance spectroscopy is used to analyze the interfacial performance and ionic conductivity of the PVDF-HFP-LLZO-TEGDME electrolyte. To calculate the Li-ion conductivity of PVDF-HFP-LLZO-TEGDME electrolytes, EIS measurements were used for generating Nyquist plots, and the ionic conductivity is calculated according to the following equation:

$$\sigma = d/AR$$

where R is the resistance, as determined from Nyquist plot fitting, d is the thickness, and A is the area of the electrolyte surface contact. The resistance R-value was calculated from the intercept of the linear fit of the straight line with the *x*-axis in Fig. 7 [39,40].

Temperature dependence of ionic conductivity with various amounts of plasticizer loading is shown in Fig. 4a, b and S8, in comparison with that of the pure PVDF-HFP (LiTFSI)-LLZO electrolyte. Pure CSEs provide an ionic conductivity of 1.2×10^{-5} at 25 °C. After the addition of the TEGDME plasticizer, the ionic conductivities of the CSEs increased and then, beyond a threshold (30 wt%), decreased again [27,41]. The high content of 30 wt% of the TEGDME liquid plasticizer enhances ionic conductivity; for example, the CSE30 exhibits an ionic conductivity of 6.2×10^{-4} and 3.6×10^{-4} S cm^{-1} at 25 and 60 °C, respectively. When TEGDME loading is equal to 30 wt%, the enhancement is attributed to (i) a decreased crystalline nature and an increase in the amorphous nature of the polymer and (ii) effective Li-ion transfer interactions between TEGDME, PVDF-HFP (LiTFSI), and the LLZO electrolyte [27,41]. Nevertheless, when the ratio increased to more than 30%, electrolyte conductivity decreased, which is attributed to poor mechanical stability based on our work and previous reports [27,42]. The electrochemical impedance study shows that ionic conductivity is enhanced by orders of magnitude upon the addition of TEGDME plasticizers (Table 1).

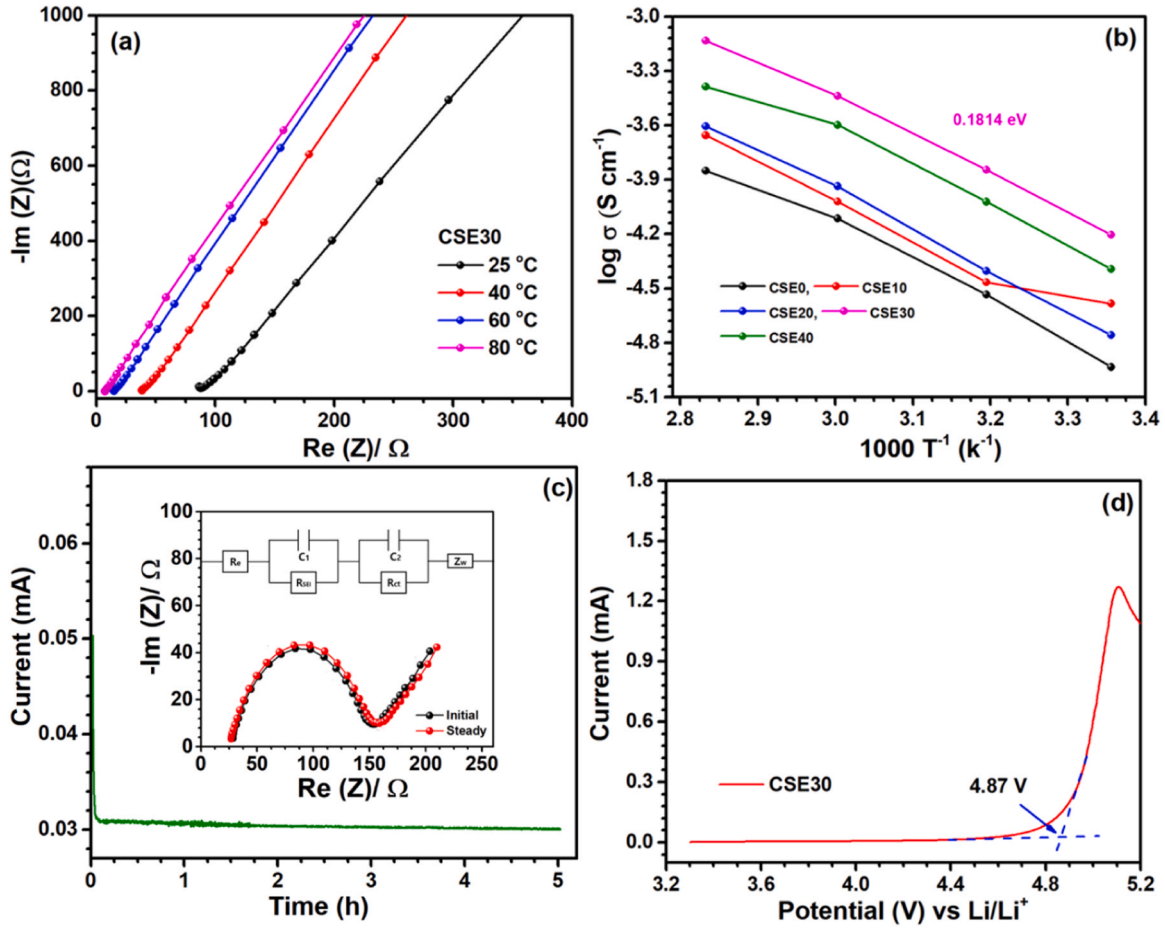

Fig. 4. (a) EIS measurements of CSE30, (b) Arrhenius plot of CSE0–40 electrolytes, (c) chronoamperometry curve of the CSE30 electrolyte and (d) Linear sweep voltammetry (LSV) of CSE30 electrolyte.

Fig. 4b displays the temperature dependence of ionic conductivity of the CSE with different TEGDME. Notably, the CSE electrolyte with 30 wt% TEGDME exhibits a high ionic conductivity for all temperatures, and the calculated activation energy was 0.1814 eV. The linear line indicates that the ions transfer in these CSEs by free diffusion rather than by a jumping motion [43]. Fig. 4c shows the chronoamperometry curve of the CSE30 non-ion blocking Li symmetric cell. The polarization voltage was 10 mV, the initial (i_o) and steady-state (is) currents were 50 µA and 30 µA, and the R_o and R_s were 122.69 Ω and 127.65 Ω, respectively. The Li^+-ion transference number (t_{Li+}) of the electrolyte was calculated based on the following equation: [44,45].

$$t_{Li+} = \frac{i_s \quad (\Delta V - i_o Ro)}{i_o \quad (\Delta V - i_s Rs)}$$

The Li-ion transference number of the CSE30 electrolyte is 0.376.

To achieve a high energy density, long life cycle, and high safety for Li-ion batteries, the electrolyte must have a wide potential window. In commonly used commercial liquid electrolytes, decomposition starts at > 4.2 V [7]. Fig. 4d shows the results of our prepared CSE in the potential range of 3–5.1 V (*vs.* Li/Li^+) with a scan rate of 1 mV s^{-1}. The oxidation current increases at 4.87 V (*vs.* Li/Li^+), indicating the CSE decomposition potential of the electrolyte. It was confirmed that the electrochemical stability increases with the addition of LLZO nanopowder, and this proves that the electrochemical stability of the CSE can be increased to an extent, which fulfills the requirements of commercial LIBs. A-Li symmetric cell was used to analyze the electrochemical stability of the PVDF-HFP-LLZO-TEGDME electrolyte with a Li-metal anode during the Li plating and stripping process at 60 °C at a current density of 0.1 mA cm^{-2}. Fig. 5a indicates the smooth voltage profile of the cell with the CSE30 electrolyte, which indicates a stable interface between the electrolyte and the Li-metal. The 30 wt% electrolytes have a lower overpotential, suggesting a lower interfacial resistance. For comparison, we have studied the Li plating and stripping performance of the different electrolytes (CSE0, 10, 20, and 40) based cells (Fig. 5b and Fig. S9). Other cell peaks were sharp and had high overpotential because of their low ionic conductivity and compatibility. Compared

Table 1
Ion conductivity of CSE0, CSE10, CSE20, CSE30, and CSE40 at different temperatures.

Temperature (°C)	Ionic conductivity of composite solid electrolyte (S cm^{-1})				
	CSE0	CSE10	CSE20	CSE30	CSE40
25	1.2×10^{-5}	2.6×10^{-5}	1.7×10^{-5}	6.2×10^{-5}	4.1×10^{-5}
40	2.9×10^{-5}	3.4×10^{-5}	3.9×10^{-5}	1.4×10^{-4}	9.5×10^{-5}
60	7.7×10^{-5}	9.5×10^{-5}	1.2×10^{-4}	3.6×10^{-4}	2.5×10^{-4}
80	1.4×10^{-4}	2.2×10^{-4}	2.5×10^{-4}	7.4×10^{-4}	4.1×10^{-4}

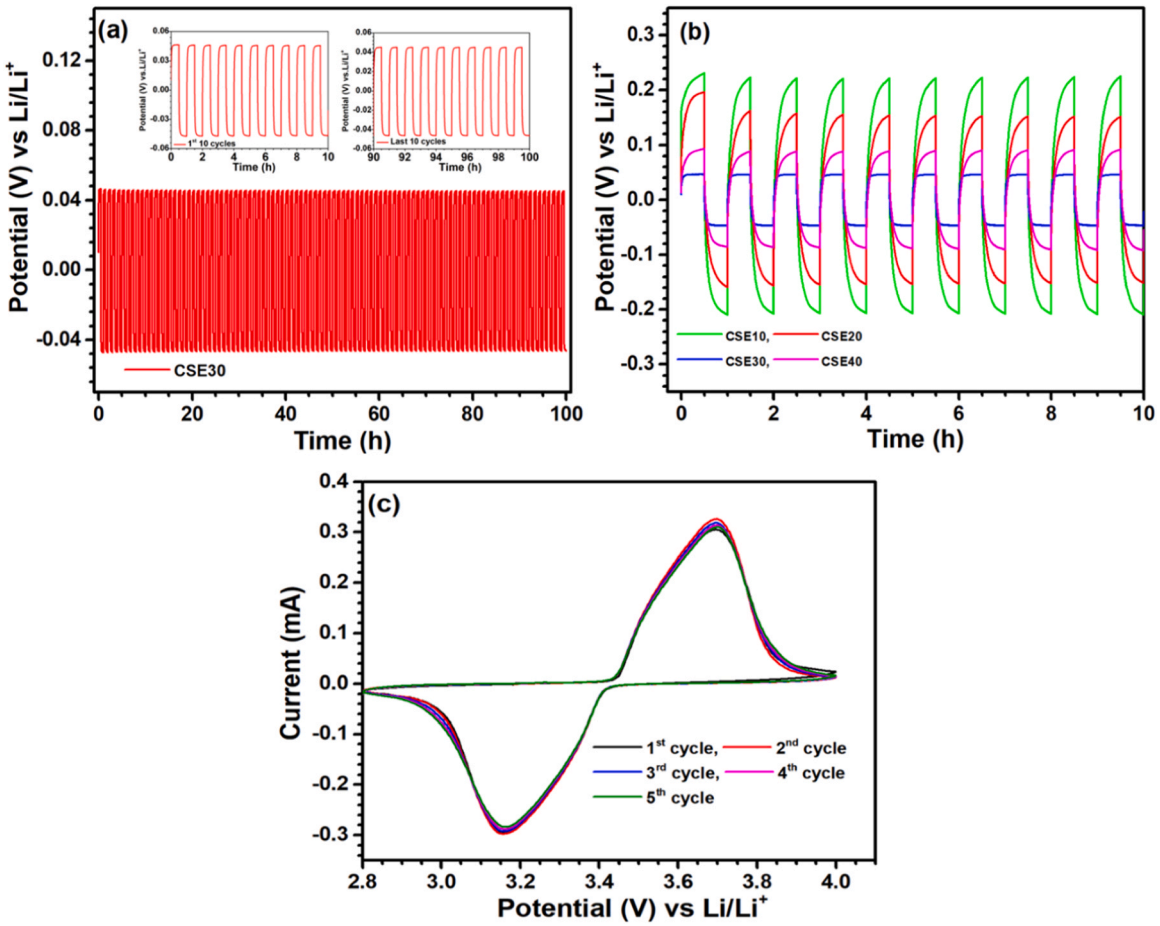

Fig. 5. (a) GCD measurement of Li symmetric cell with CSE30 electrolyte (inset image: First 10 cycles and last 10 cycles), (b) Comparison of GCD measurement of Li symmetric cell with CSE0–40 electrolytes and (c) Cyclic voltammetry of the Li/CSE30/$LiFePO_4$ cell at a scan rate of 0.1 mV S^{-1}. Electrochemical performance of the cell was tested at 60 °C.

to others, the CSE30 Li metal symmetric cell confirms the Li stability nature of the electrolytes. The electrochemical stability window of the electrolyte is a vital parameter for electrochemical studies. Further, the tensile strength was studied to understand the mechanical properties of the electrolyte. Fig. S10 displays the stress-strain curves of CSE30 electrolytes before and after the cycling test. It was confirmed that the CSE30 electrolyte before and after cycling possessed a tensile strength of 4.15 MPa with 250% strain and 3 MPa with 370% strain, respectively, which indicates that the cycled electrolytes tensile strength is slightly weaker than the pristine one. But the mechanical strength of the electrolyte is still good for long battery cycle life performance.

4.2. Charge/discharge performance of a Li-ion solid-state battery

The Li/$LiFePO_4$ cell was assembled using PVDF-HFP (LiTFSI) – 10% LLZO – 30% TEGDME SEs to form a solid-state battery (SSB) at 60 °C for cell testing. Fig. S11 shows electrochemical impedance spectra of the Li/CSE30/ $LiFePO_4$ cell at 60 °C. The charge-transfer resistance of the cell is 23.57 Ω, and it indicates good interfacial compatibility between the electrode and electrolyte materials. The low charge transfer resistance is a benefit for the fast charge-discharge process of the ASSLIB. The CSE has good compatibility and is attached well to the cathode composite. The cyclic voltammetry curve of the first 5 cycles of the cell is shown in Fig. 5c. The two characteristic peaks of oxidation at 3.69 V and the reduction peak at 3.15 V are due to charge and discharge processes.[46] No other peaks could be observed in the CV curve, which indicates that no side reactions happen in the cell process. Different CV cycle curves overlap, which implies that the cell has a high reversible behavior and excellent interface stability [46]. Fig. 6a shows the charge/discharge performance of the cell for the selected cycles. The initial discharge capacity of the cell was 157 mAh g^{-1}, and the coulombic efficiency of the cell was > 99%. For comparison, we added the liquid cell test in Fig. S12. After 20 cycles, the capacity of the cell increased to 169 mAh g^{-1} due to the activation process of the cell. Fig. 6b shows the cycle stability of the SSB at a 0.1 C rate. It can be seen that the discharge capacity of the cell decreased to 150 mAh g^{-1} after 100 cycles. The capacity loss was 0.21% per cycle based on the 20th cycle (high capacity). It is worth mentioning that the capacity loss was low and that capacity retention was 88.75%. This indicates that our prepared solid electrolyte is an effective candidate for an all-solid-state LIB. For comparison, we studied the cycling performance test for different electrolyte (CSE0, 10, 20, and 40) based cells (Fig. 6c and S13). The initial discharge capacities were 95, 128, 146, and 162 mAh g^{-1} at a 0.1 C rate. Expect CSE40 and other cells capacities were lower than CSE30 cells. But after a few cycles, the discharge capacity of the CSE40 cell was decreased due to low ionic conductivity and the Li-ion blocking nature of the excess plasticizer [42,47,48].

Fig. S14 (a-c) shows the cross-sectional FE-SEM image of the LFP cathode with different mass loading percentages. We studied the cycling performance test with different mass loading of LFP (2.41, 3.64, 5.61, and 6.14 mg cm^{-2}) based cells (Fig. S15 a-d). The cells delivered the initial discharge capacities of 162, 162, 144, and 138 mAh g^{-1} at a 0.1 C rate. The capacity of the cells was decreased due to Li-ion irreversibility nature and contact loss. After 50 cycles, the capacity of the cells was 147, 147, 141, and 127 mAh $g^{-1,}$ and the capacity retentions were 90.7%, 90.7%, 97.9%, and 92%. At high

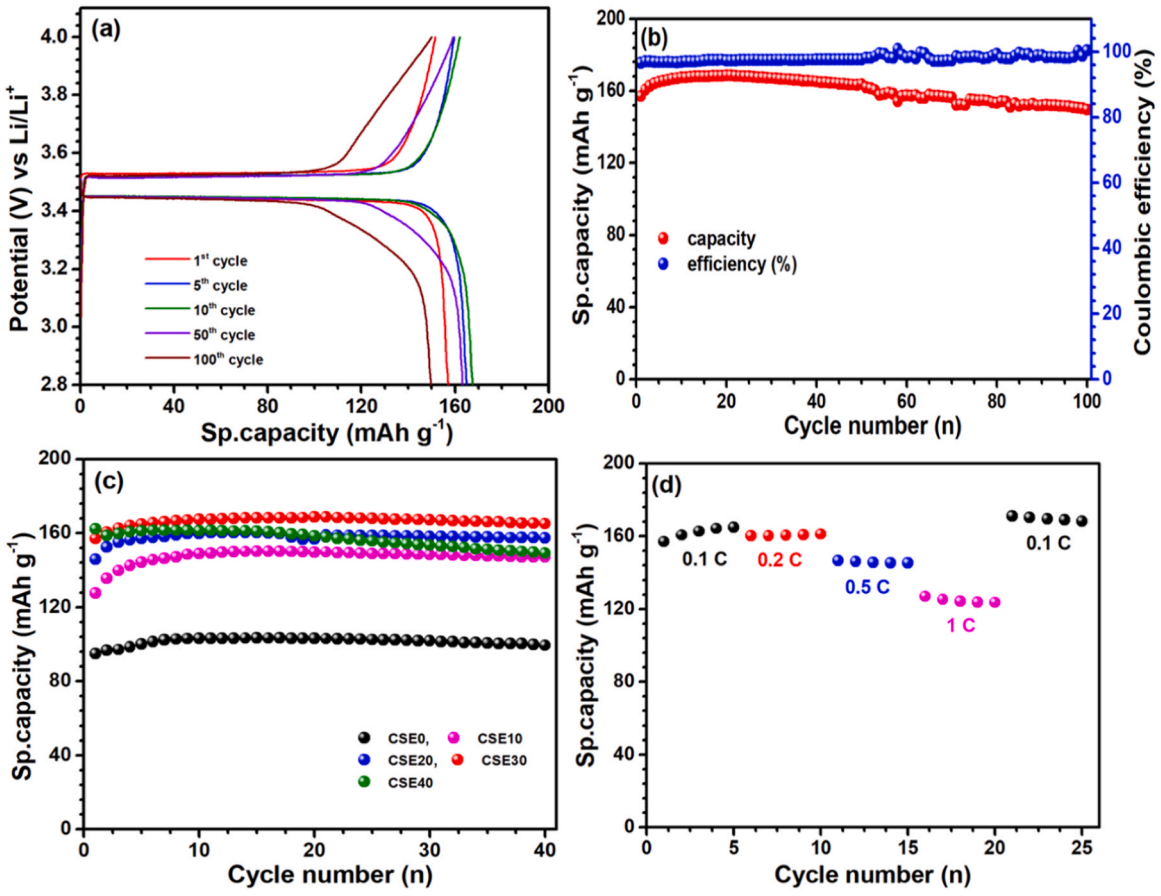

Fig. 6. (a) Galvanostatic charge-discharge curve of the selected cycles, (b) cycle stability test under 0.1 C rate, (c) Comparison graph for the cycle stability test of the different electrolyte based cells (CSE0–40) and (d) Rate capability curve of the Li/CSE30/$LiFePO_4$ cell. Electrochemical performance of the cell was tested at 60 °C.

Table 2
Comparison of electrochemical performances for the $LiFePO_4$ cathode materials associated with composite solid electrolytes.

Electrolytes	Electrochemical Performance	Cycle retention	Ref.
PVdF-HFP/TEGDME/LLZO	157 mAh g^{-1} under 0.1 C at 60 °C	88.7% after 100 cycles	This work
PVdF-HFP/LATP + PC solvent	148 mAh g^{-1} under 0.2 C at 25 °C	87.8% after 50 cycles	[43]
PVdF-HFP/LLZTO/SN + liquid electrolyte	152.8 mAh g^{-1}under 0.2 C at 25 °C	98.5% after 105 cycles	[46]
PVdF-HFP/LLZO + liquid electrolyte	113 mAh g^{-1} under 0.5 C at 25 °C	92.5% after 180 cycles	[49]
PVdF-HFP/ 1 M LiTFSI	150.7 mAh g^{-1} under 0.5 C at 70 °C	98.7% after 100 cycles	[50]
PVdF-HFP/LLZTO	133.4 mAh g^{-1} under 0.5 C at 60 °C	99.4% after 200 cycles	[51]
PVdF-HFP /PEGDA + 1 M $LiPF_6$ (EC/PC/EMC)	140 mAh g^{-1} under 0.5 C at 25 °C	97.9% after 200 cycles	[52]
PVdF-HFP/LLZTO/$LiClO_4$/EC + 1 M $LiPF_6$ (EC/PC/EMC)	152.2 mAh g^{-1} under 0.5 C at 30 °C	84.6% after 200 cycles	[53]
PVDF/PEO/LATP/$LiPF_6$	140 mAh g^{-1} under 0.1 C at 25 °C	94% after 500 cycles	[54]
PEO/LAGP/LiTFSI	135 mAh g^{-1} under 0.1 C at 50 °C	95.5% after 40 cycles	[55]
PEO(LiTFSI)/LAGP	150 mAh g^{-1} under 0.1 C at 60 °C	97.2% after 100 cycles	[56]
LLZAO-PEO/$LiClO_4$	143.8 mAh g^{-1} under 1 C at 60 °C	86% after 200 cycles	[57]
PEO/LiTFSI	134 mAh g^{-1} under 0.2 C at 60 °C	91.3% after 100 cycles	[58]
PEO(LiTFSI)	145 mAh g^{-1} under 0.1 C at 25 °C	98% after 200 cycles	[59]
PEO(LiTFSI)/LLZTO	139.1 mAh g^{-1} under 0.2 C at 55 °C	93.6% under 0.5 C after 100 cycles	[60]
PEO(LiTFSI)/ LATP/PAN	144 mAh g^{-1} under 0.2 C at 60 °C	–	[61]

loading mass, the capacity of the cell is decreased because of the low utilization of the active material. In Table 2, we compare our electrochemical cell performance with others reported work [43,46,49–61]. Fig. 6d show the rate performance of the Li/CSE30/$LiFePO_4$ cell between 0.1 and 1 C (1 C = 160 mAh g^{-1}). The first discharge capacities are 157, 160, 147, and 127 mAh g^{-1} at 0.1, 0.2, 0.5, and 1 C, respectively. At high current densities, the polarization of the cell increases, leading to a capacity decay in the discharge process. Li-ion diffusion is restricted at the electrode/electrolyte interface at high current densities, which is the main reason for the low capacity. In our work, the TEGDME plasticizer was used to enhance the Li-ion conduction at the electrode/electrolyte interface, to increase retention capacity and cell life cycle [27].

In Fig. 7a and b, we analyzed the charge/discharge performance of the cell under 1 C-rate, and the cell exhibited the initial discharge capacity of 131 mAh g^{-1}, with coulombic efficiency of > 99%. After 300 cycles, the capacity is decreased to 100 mAh g^{-1} with a capacity retention of 76.3%. Fig. 7c-f shows the electrochemical performance of the cell under a 2 C rate in the potential range of 2.8–4 V (*vs.* Li/Li^+) and 2.8–4.1 V (*vs.* Li/Li^+). The cell tested in the potential window of 2.8–4 V (*vs.* Li/Li^+) provided the initial discharge capacity of 107 mAh g^{-1}; nevertheless, the capacity of the cell gradually decreased

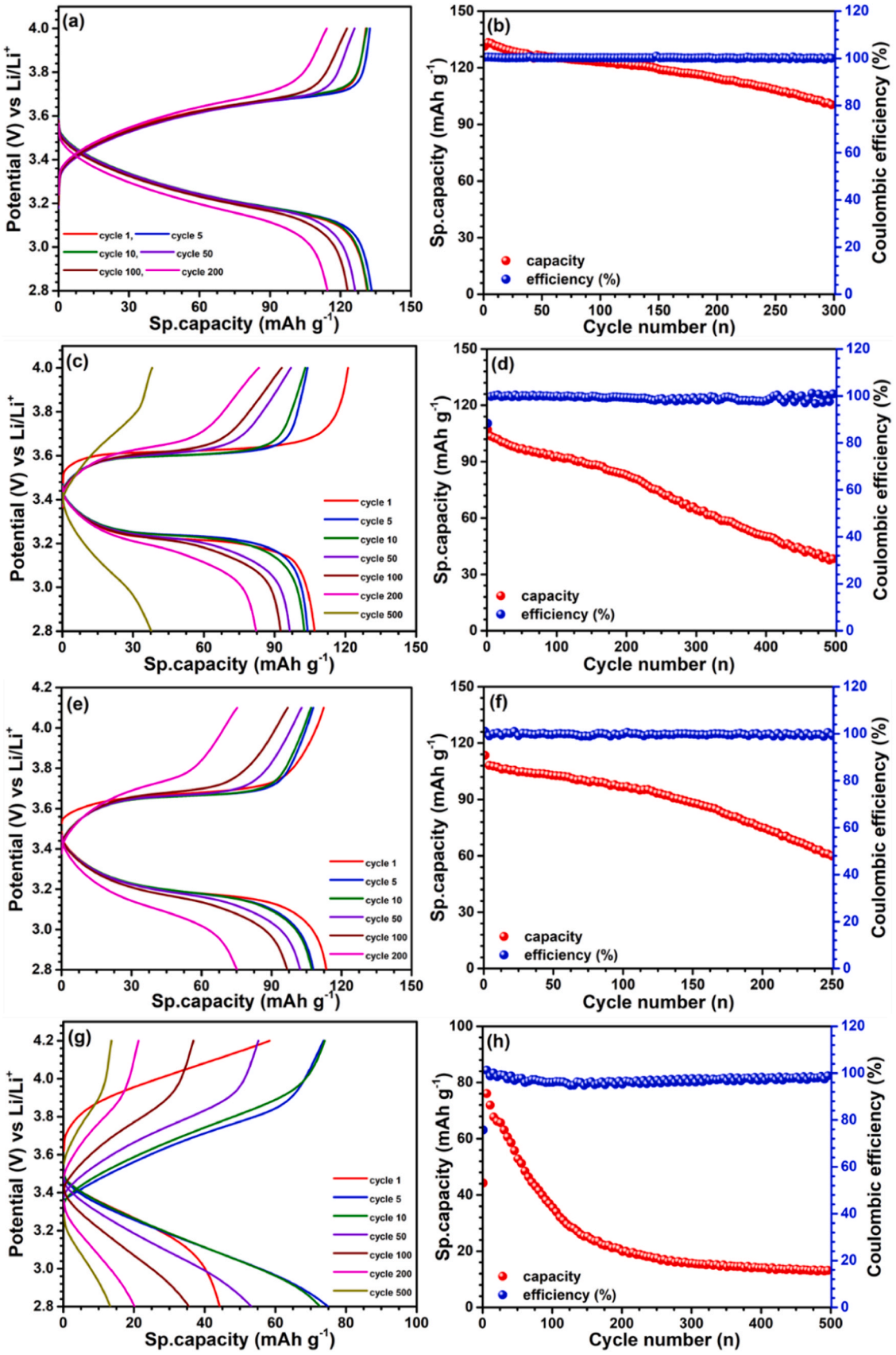

Fig. 7. (a) Galvanostatic charge-discharge curve of the selected cycles, (b) cycle stability test under 1 C rate, (c) Galvanostatic charge-discharge curve of the selected cycles, (d) cycle stability test under 2 C rate, (e) Galvanostatic charge-discharge curve of the selected cycles, (f) cycle stability was studied in the potential range of 2.8–4.1 V with a current density of 2 C, (g) Galvanostatic charge-discharge curve of the selected cycles and (h) cycle stability was studied in the potential range of 2.8–4.2 V with a current density of 3 C. Electrochemical performance of the cell was tested at 60 °C.

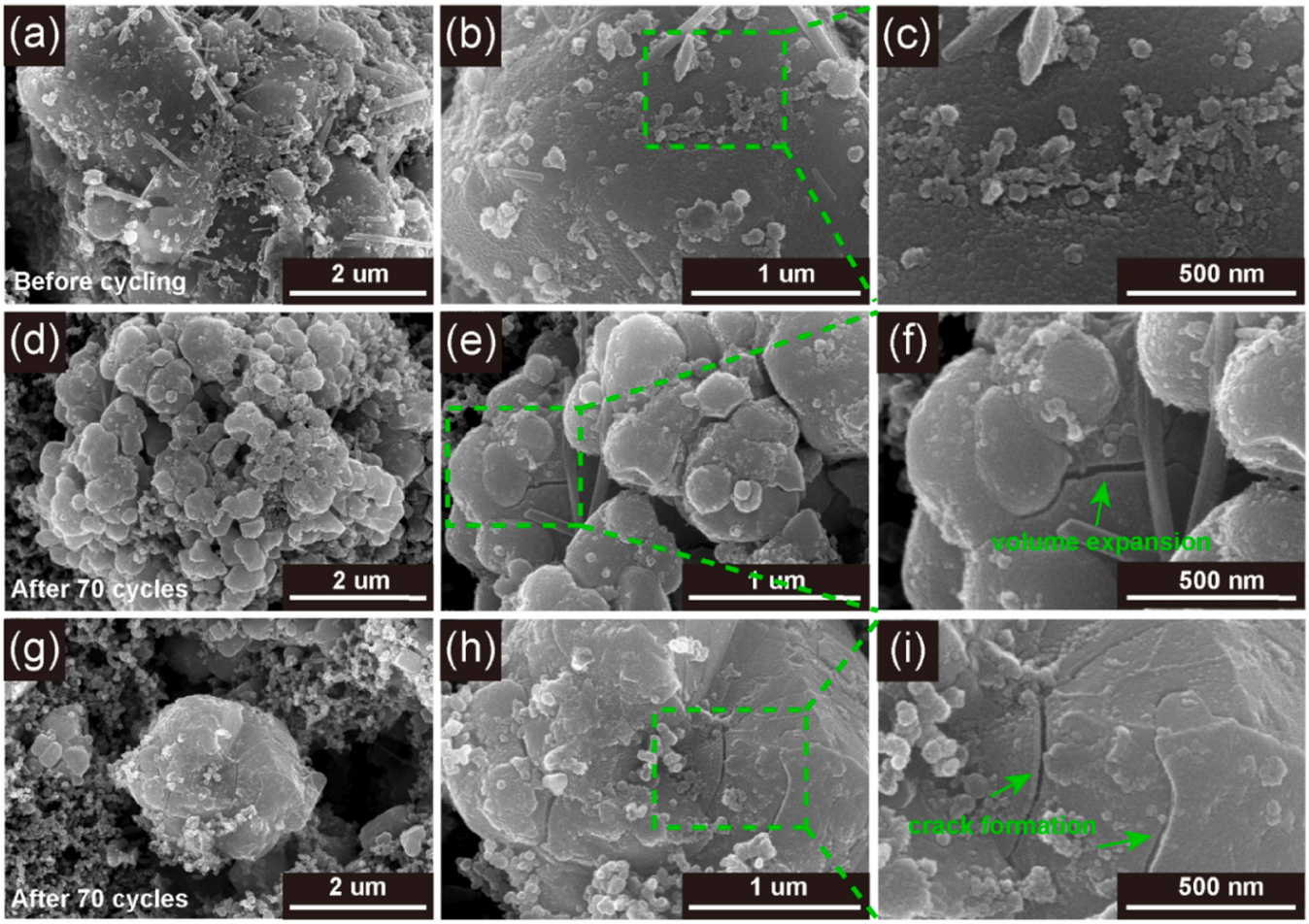

Fig. 8. FE-SEM image of the $LiFePO_4$ electrode particles. (a-c) Before cycle test and (d-i) After 70 cycles.

because of the fast the charge-discharge process. After 250 cycles, the cell retains 69% of its initial discharge capacity. Compared to this, the cell evaluated between 2.8 and 4.1 V (*vs.* Li/Li^+) delivered a higher discharge capacity (113 mAh g^{-1}), but the capacity of the cell is drastically reduced as a result of the Li-ion irreversibility, and the capacity retention of the cell is found to be only 53%. Additionally, the electrochemical performance of the Li/CSE30/$LiFePO_4$ cell was tested under 3 C in the potential range of 2.8–4.2 V (*vs.* Li/Li^+) (Fig. 7g-h). The initial discharge capacity of the cell is 44 mAh g^{-1}, and after 250 cycles, the capacity is severely declined to 17 mAh g^{-1} due to the poor Li-ion irreversibility and electrolyte decomposition. Compared to Li/CSE30/SS asymmetric cell, the Li/CSE30/$LiFePO_4$ cell is stable up to 4.2 V (*vs.* Li/Li^+) because the long-term cycle life induces the electrolyte decomposition at a higher voltage. Furthermore, the capacity loss is due to minimum contact loss between the active materials in the cathode composite. To further enhance the capacity and the life cycle of the SSB, high-voltage cathode materials (NCM and NCA) and ionic liquids in the cathode/electrolyte interface will be used [41,62]. Hence, PVDF-HFP (LiTFSI) - 10% LLZO - 30% TEGDME is the best candidate for next-generation solid-state Li-metal batteries.

4.3. Li-ion conduction mechanism in composite solid electrolyte

Fig. S16 shows the plasticizer/polymer matrix bond formation and Li-ion conduction mechanism in the composite solid electrolyte. Fig. S16a shows the FTIR spectra for PVDF-HFP films with different wt% of TEGDME plasticizers. The C-O bond peak at around 1100 cm^{-1}, and CH_2-CH_2 long-chain band evolved in the PVDF-HFP film concerning increasing the quantity of TEGDME plasticizer [63,64]. The - O-CH_3 group in TEGDME is making a bond with -CH_2-CF_2- (-VDF crystalline group) in the PVDF-HFP polymer matrix and then decreases its crystalline nature of the film (Fig. S17) [65]. Generally, the amorphous nature of the film increases the ionic conductivity of the electrolyte. Fig. S16b, c, and S18 show the XPS spectra for the CSE30 composite solid electrolyte. The carbon spectra show a very broad peak, which after deconvolution, is attributed to C-O, C-C/C-H, C-CF, C-F, C-F_2, and CF_3 at 283.69, 285.78, 287.07, 289.61, 290.93, and 292.65 eV [66,67]. The peak at 283.69 eV further confirmed the presence of –O-C (-O- CH_3 in TEGDME plasticizer) in the CSE. The fluorine spectra were broad, which confirms the presence of more than one chemical state of F in the electrolyte. After deconvolution, the peak at 685.17 eV corresponded to the Li-F bond [67]. It is confirmed that the Li-ion migration in the PVDF-HFP electrolyte by Li-F segmental motion in the electrolyte (Fig. S16d) [68–71]. Overall, the experimental results concluded that the TEGDME plasticizer in the composite solid electrolyte decreased the crystalline nature of the film, and the Li-ion migrates in the electrolyte by Li-F segmental motion.

4.4. Post-modem analysis of $LiFePO_4$ electrode and CSE30 electrolyte

For further understanding, the post-modem analysis of the electrode explains the reasons for the capacity loss and irreversibility of the cell. Fig. 8 shows the FE-SEM image of the $LiFePO_4$ electrode before and after 70 cycles. Before cycling, the $LiFePO_4$ particle surface looks smooth, and there is no crack formation on the particle (Fig. 8a-c). But after 70 cycles, very small cracks formed on

the surface of the $LiFePO_4$ cathode particles (Fig. 8d-i). We further compared the TEM images of before and after cycled $LiFePO_4$ particles. Fig. S19 shows TEM and HR-TEM images of the $LiFePO_4$ electrode before and after 70 cycles. Figure S19h shows the crack developed on the surface of the $LiFePO_4$ particles. Importantly primary-like particles remained well-intact, but some cracks developed on the $LiFePO_4$ particle surface. The repeated charge/discharge process may induce the volume expansion of the particles, which leads to the formation of the crack on the surface.

Figure S20 shows the XPS spectra for the $LiFePO_4$ electrode before and after 100 cycles. After cycling, the Li 1 s and Fe 2p peak spectra slightly shifted, and peaks became broader due to differential charging states of the surface. In addition, a peak shoulder appeared at 715.65 and 718.05 eV after 70 cycles, which corresponds to the satellite peak of Fe^{3+} ion [72]. The main reason for the marginal capacity loss is due to the volume expansion and irreversibility of the $LiFePO_4$. Additionally, the XPS analysis was used to study the electrochemical cycled CSE30 electrolyte. After 100 cycles, the carbon peak was marginally shifted due to the charge/discharge process (Fig. S21). The Li 1 s spectra were large, which indicates the presence of more than one chemical state of Li in the CSE. After deconvolution, two chemical states of surface Li atoms were revealed: Li-N bond for LiTFSI salt at 55.06 eV and Li-O bond for LLZO ceramic filler at 52.21 eV (Fig. S18 b). After the electrochemical cycling, the surface Li 1 s spectra were absent due to Li-ion depletion layer formation on the CSE surface (Fig. S21 b). The main reason for the degradation is C 1 s spectra shifting and the absence of Li 1 s spectra on the surface of CSE. Raman spectroscopy was used to investigate chemical bonding and intramolecular bonds. Fig. S20 a shows the disorder carbon band (I_D) at 1350 cm^{-1} and ordered graphitic band (I_G) at 1595 cm^{-1} of the cycled LFP cathode composite, which corresponds to the presence of amorphous carbon in the form of conductive additive. (Fig. S22). Furthermore, spectroscopy was used to analyze the CSE30 before and after cycling performance (Fig. S22 b-c). The Raman spectroscopy has not detected any signal because the CSE signal intensity is very weak. The peak was very broad, and there was no change in before and after cycling performance.

5. Conclusion

In this work, a CSE based on PVDF-HFP-10% LLZO - (different wt%) TEGDME was successfully prepared *via* cost-effective solution casting or the phase-inversion method. The addition of a liquid plasticizer in the form of 30% TEGDME CSE can enhance the electrochemical performance of the CSE, provide excellent flexibility, mechanical and thermal stability, a wide potential window (> 4 V), and high ionic conductivity (1.2×10^{-4} at 60 °C). The Li symmetric cell with CSE 30% can be cycled by Li plating/striping for 100 h without a short circuit. The charge-transfer resistance of the cell is 23.57 Ω, and it is good for the fast charge/discharge process. The Li/CSE30/$LiFePO_4$ cell shows a high discharge capacity of 150 mAh g^{-1} at a 0.1 C rate after 100 cycles. Moreover, the ASSLIB provided the discharge capacity of 100 mAh g^{-1} at a 1 C rate after 300 cycles and 74 mAh g^{-1} at a 2 C rate after 250 cycles. The $-O-CH_3$ group in the TEGDME plasticizer makes a bond with the $-CH_2-CF_2-$ crystalline group, then increases the amorphous nature and enhances the ionic conductivity of the electrolyte. The XPS results confirm the Li-ion migrates in the PVDF-HFP matrix by Li–F segmental motion. Furthermore, the SSB provides a high discharge capacity even at high current densities. It is believed that this CSE has the potential to be applied in numerous power sources, such as LIBs, Li-S batteries, and supercapacitors.

CRediT authorship contribution statement

Seol Jae-chang & Balasubramaniam Ramkumar: Conceptualization, Methodology, Validation, Formal analysis, Data curation, Writing - original draft, Visualization. **Vanchiappan Aravindan**: Writing – review & editing, Supervision. **Thangavel Ranjith**: Writing – review & edition. **Yun-Sung Lee**: Supervision, Resources, Funding acquisition, Project administration.

Data availability

The data that has been used is confidential.

Declaration of Competing Interest

The authors declare that they have no known competing financial interests or personal relationships that could have appeared to influence the work reported in this paper.

Acknowledgment

The author would like to thank Jeong Kwan.Co. Ltd for their consistent support. YSL acknowledges the financial support from the National Research Foundation of Korea (NRF) grant funded by the Korean government (Ministry of Science, ICT & Future Planning) (No. 2019R1A2C1007620). VA acknowledges financial support from the Science and Engineering Research Board, a statutory body of the Department of Science and Technology, Govt. of India, through Swarnajayanti Fellowship (SB/SJF/2020–21/12).

Appendix A. Supporting information

Supplementary data associated with this article can be found in the online version at doi:10.1016/j.jallcom.2022.167077.

References

[1] K. Huang, Y. Wang, M. Mi, D. Ma, B. Yong, P. Zhang, BF4-modified PVDF-HFP composite polymer electrolyte for high-performance solid-state lithium metal battery, J. Mater. Chem. A 8 (2020) 20593–20603, https://doi.org/10.1039/d0ta08169h

[2] B. Ramkumar, S. Yuvaraj, S. Surendran, K. Pandi, Y.S. Hari Vignesh Ramasamy, Lee R. Kalai Selvan, Synthesis and characterization of carbon coated $LiCo_{1/3}Ni_{1/3}Mn_{1/3}O_2$ and bio-mass derived graphene like porous carbon electrodes for aqueous Li-ion hybrid supercapacitor, J. Phys. Chem. Solids 112 (2018) 270–279, https://doi.org/10.1016/j.jpcs.2017.09.012

[3] H.V. Ramasamy, S. Sinha, J. Park, M. Gong, V. Aravindan, J. Heo, Y.S. Lee, J Enhancement of electrochemical activity of ni-rich $LiNi_{0.8}Mn_{0.1}Co_{0.1}O_2$ by precisely controlled Al2O3 nanocoatings via atomic layer deposition, Electrochem Sci. Technol. 10 (2019) 196–205, https://doi.org/10.5229/JECST.2019.10.2.196

[4] S.B. Lee, B. Ramkumar, Double-shelled hybrid $MgFe_2O_4/Fe_2O_3$ hollow microspheres as a high-capacity anode for lithium-ion batteries, J. Ind. Eng. Chem. 110 (2022) 262–273, https://doi.org/10.1016/j.jiec.2022.03.001

[5] B. Ramkumar, K. So-young, N. Chan-woo, V. Aravindan, Y.S. Lee, LiBO2-modified LiCoO2 as an efficient cathode with garnet framework Li6.75La3Zr1.75Nb0.25O12 electrolyte toward building all-solid-state lithium battery for high-temperature operation, Article. 136955, Electro Acta 359 (2020), https://doi.org/10.1016/j.electacta.2020.136955

[6] B. Wu, S. Wang, W.J. Evans, D.Z. Deng, J. Yang, J. Xiao, Interfacial behaviours between lithium ion conductors and electrode materials in various battery systems, J. Mater. Chm A. 4 (2016) 15266–15280, https://doi.org/10.1039/c6ta05439k

[7] J. Li, L. Zhu, J. Zhang, M. Jing, S. Yao, X. Shen, S. Li, F. Tu, Approaching high performance PVDF-HFP based solid composite electrolytes with LLTO nanorods for solid-state lithium-ion batteries, Int J. Energy Res (2021) 1–12, https://doi.org/10.1002/er.6347

[8] D. Cao, X. Sun, Q. Li, A. Natan, P. Xiang, H. Zhu, Lithium dendrite in all-solid-state batteries: growth mechanisms, suppression strategies, and characterizations, Matter 3 (2020) 57–94, https://doi.org/10.1016/j.matt.2020.03.015

[9] X. Shen, R. Zhang, X. Chen, X.B. Cheng, X. Li, Q. Zhang, The failure of solid electrolyte interphase on Li metal anode: structural uniformity or mechanical strength, Adv. Energy Mater. 10 (2020) 1–8, https://doi.org/10.1002/aenm.201903645

[10] H.J. Choi, S.Y. Kim, M.K. Gong, H. Vignesh, V. Aravindan, Y.G. Lee, Y.S. Lee, Tailored perovskite Li0.33La0.56TiO3 via an adipic acid-assisted solution process: A promising solid electrolyte for lithium batteries, J. Alloy. Compd. 729 (2017) 338–343, https://doi.org/10.1016/j.jallcom.2017.09.160

[11] A. Manthiram, X. Yu, S. Wang, Lithium battery chemistries enabled by solid-state electrolytes, Nat. Rev. Mater. 2 (2017) 1–16, https://doi.org/10.1038/natrevmats.2016.103

[12] B. Ramkumar, C.W. Nam, V. Aravindan, D. Eum, K. Kang, Y.S. Lee, Interfacial engineering in a cathode composite based on garnet-type solid-state Li-ion battery with high voltage cycling, ChemElectroChem 8 (2021) 570–576, https://doi.org/10.1002/celc.202001116

[13] S. Amaresh, K. Karthikeyan, K.J. Kim, Y.G. Lee, Y.S. Lee, Aluminum based sulfide solid lithium ionic conductors for all solid state batteries, Nanoscale 6 (2014) 6661–6667, https://doi.org/10.1039/c4nr00804a

[14] Y. Meesala, A. Jena, H. Chang, R.S. Liu, Recent advancements in Li-ion conductors for all-solid-state Li-ion batteries, ACS Energy Lett. 2 (2017) 2734–2751, https://doi.org/10.1021/acsenergylett.7b00849

[15] S.A. Pervez, M.A. Cambaz, V. Thangadurai, M. Fichtner, Interface in solid-state lithium battery: challenges, progress, and outlook, ACS Appl. Mater. Interfaces 11 (2019) 22029–22050, https://doi.org/10.1021/acsami.9b02675

[16] M. Dirican, C. Yan, P. Zhu, X. Zhang, Composite solid electrolytes for all-solid-state lithium batteries, Mater. Sci. Eng. R. Rep. 136 (2019) 27–46, https://doi.org/10.1016/j.mser.2018.10.004

[17] S. Xia, X. Wu, Z. Zhang, Y. Cui, W. Liu, Practical challenges and future perspectives of all-solid-state lithium-metal batteries, Chem 5 (2019) 753–785, https://doi.org/10.1016/j.chempr.2018.11.013

[18] S. Chintapalli, R. Frech, Effect of plasticizers on ionic association and conductivity in the (PEO)9LiCF3SO3 system, Macromolecules 29 (1996) 3499–3506, https://doi.org/10.1021/ma9515644

[19] J. Lu, Y. Liu, P. Yao, Z. Ding, Q. Tang, J. Wu, Z. Ye, K. Huang, X. Liu, Hybridizing poly (vinylidene fluoride-co-hexafluoropropylene) with Li6.5La3Zr1.5Ta0.5O12 as a lithium-ion electrolyte for solid state lithium metal batteries, Chem. Eng. J. 367 (2019) 230–238, https://doi.org/10.1016/j.cej.2019.02.148

[20] H. Xie, Z. Tang, Z. Li, Y. He, Y. Liu, H. Wang, PVDF-HFP composite polymer electrolyte with excellent electrochemical properties for Li-ion batteries, J. Solid State Electrochem 12 (2008) 1497–1502, https://doi.org/10.1007/s10008-008-0511-9

[21] W. Xiao, X. Li, H. Guo, Z. Wang, Y. Zhang, X. Zhang, Preparation of core-shell structural single ionic conductor SiO 2@Li+ and its application in PVDF-HFP-based composite polymer electrolyte, Electro Acta 85 (2012) 612–621, https://doi.org/10.1016/j.electacta.2012.08.120

[22] C.C. Yang, Z.Y. Lian, S.J. Lin, J.Y. Shih, W.H. Chen, Preparation and application of PVDF-HFP composite polymer electrolytes in $LiNi_{0.5}Co_{0.2}Mn_{0.3}O_2$ lithium-polymer batteries, Electro Acta 134 (2014) 258–265, https://doi.org/10.1016/j.electacta.2014.04.100

[23] Z. Yang, H. Peng, W. Wang, T. Liu, Crystallization behavior of poly(ε-caprolactone)/layered double hydroxide nanocomposites, J. Appl. Polym. Sci. 116 (2010) 2658–2667, https://doi.org/10.1002/app

[24] J.M.C. Puguan, W.J. Chung, H. Kim, Ion-conductive and transparent PVdF-HFP/silane-functionalized ZrO_2 nanocomposite electrolyte for electrochromic applications, Electro Acta 196 (2016) 236–244, https://doi.org/10.1016/j.electacta.2016.02.172

[25] R. Murugan, V. Thangadurai, W. Weppner, Fast lithium ion conduction in garnet-type $Li_7La_3Zr_2O_{12}$, Angew Chemie - Int Ed 46 (2007), pp. 7778–7781, https://doi.org/10.1002/anie.200701144

[26] T. Liu, Y. Zhang, X. Zhang, L. Wang, S.X. Zhao, Y.H. Lin, Y. Shen, J. Luo, L. Li, C.W. Nan, Enhanced electrochemical performance of bulk type oxide ceramic lithium batteries enabled by interface modification, J. Mater. Chem. A 6 (2018) 4649–4657, https://doi.org/10.1039/c7ta06833f

[27] J. Zheng, H. Dang, X. Feng, P.H. Chien, Y.Y. Hu, Li-ion transport in a representative ceramic-polymer-plasticizer composite electrolyte: $Li_7La_3Zr_2O_{12}$-polyethylene oxide-tetraethylene glycol dimethyl ether, J. Mater. Chem. A 5 (2017) 18457–18463, https://doi.org/10.1039/c7ta05832b

[28] R. Thangavel, K. Kaliyappan, H.V. Ramasamy, X. Sun, Y.S. Lee, Engineering the pores of biomass-derived carbon: insights for achieving ultrahigh stability at high power in high-energy supercapacitors, ChemSusChem 10 (2017) 2805–2815, https://doi.org/10.1002/cssc.201700492

[29] D. Mazza, Remarks on a ternary phase in the La_2O_3-Me_2O_5-Li_20 system (Me = Nb, Ta), Mater. Lett. 7 (1988) 205–207.

[30] J. Zheng, M. Tang, Y.Y. Hu, Lithium ion pathway within $Li_7La_3Zr_2O_{12}$ -polyethylene oxide composite electrolytes, Angew. Chem. 128 (2016) 12726–12730, https://doi.org/10.1002/ange.201607539

[31] P.M. Shanthi, P.J. Hanumantha, T. Albuquerque, B. Gattu, P.N. Kumta, Novel composite polymer electrolytes of PVdF-HFP derived by electrospinning with enhanced Li-ion conductivities for rechargeable lithium-sulfur batteries, ACS Appl. Energy Mater. 1 (2018) 483–494, https://doi.org/10.1021/acsaem.7b00094

[32] Y.F. Liang, Y. Xia, S.Z. Zhang, X.L. Wang, X.H. Xia, C.D. Gu, J.B. Wu, J.P. Tu, A preeminent gel blending polymer electrolyte of poly(vinylidene fluoride-hexafluoropropylene) -poly(propylene carbonate) for solid-state lithium ion batteries, Electro Acta 296 (2019) 1064–1069, https://doi.org/10.1016/j.electacta.2018.11.182

[33] Shalu, V.K. Singh, R.K. Singh, Development of ion conducting polymer gel electrolyte membranes based on polymer PVdF-HFP, BMIMTFSI ionic liquid and the Li-salt with improved electrical, thermal and structural properties, J. Mater. Chem. C. 3 (2015) 7305–7318, https://doi.org/10.1039/c5tc00940e

[34] L.J. Hardwick, J.A. Saint, I.T. Lucas, M.M. Doeff, R. Kostecki, FTIR and raman study of the $Li_xTi_yMn_{1-y}O_2$ (y=0, 0.11) cathodes in methylpropyl pyrrolidinium Bis (fluoro-sulfonyl)imide, LiTFSI electrolyte, J. Electrochem Soc. 156 (2009) A120–A127, https://doi.org/10.1149/1.3040210

[35] S. Ferrari, E. Quartarone, C. Tomasi, M. Bini, P. Galinetto, M. Fagnoni, P. Mustarelli, Investigation of ether-based ionic liquid electrolytes for lithium-O_2 batteries, J. Electrochem Soc. 162 (2015) A3001–A3006, https://doi.org/10.1149/2.0011502jes

[36] M. Kerner, N. Plylahan, J. Scheers, P. Johansson, Thermal stability and decomposition of lithium bis(fluorosulfonyl)imide (LiFSI) salts, RSC Adv. 6 (2016) 23327–23334, https://doi.org/10.1039/c5ra25048j

[37] K. Huang, Y. Wang, H. Mi, D. Ma, B. Yong, P. Zhang, BF_4-modified PVDF-HFP composite polymer electrolyte for high-performance solid-state lithium metal battery, J. Mater. Chem. A 8 (2020) 20593–20603, https://doi.org/10.1039/d0ta08169h

[38] X. Zhang, T. Liu, S. Zhang, X. Huang, B. Xu, Y. Lin, B. Xu, L. Li, C.W. Nan, Y. Shen, Synergistic coupling between Li6.75La3Zr1.75Ta0.25O12 and poly(vinylidene fluoride) induces high ionic conductivity, mechanical strength, and thermal stability of solid composite electrolytes, J. Am. Chem. Soc. 139 (2017) 13779–13785, https://doi.org/10.1021/jacs.7b06364

[39] H. Li, Electrochemical impedance spectroscopy study on using Li10GeP2S12 electrolyte for all-solid-state lithium batteries, Article. 210229, Int J. Electrochem Sci. 16 (2021), https://doi.org/10.20964/2021.02.33

[40] W. Choi, H.C. Shin, J.M. Kim, J.Y. Choi, W.S. Yoon, Modeling and applications of electrochemical impedance spectroscopy (Eis) for lithium-ion batteries, J. Electrochem Sci. Technol. 11 (2020) 1–13, https://doi.org/10.33961/jecst.2019.00528

[41] Z. Xue, D. He, X. Xie, Poly(ethylene oxide)-based electrolytes for lithium-ion batteries, J. Mater. Chem. A 3 (2015) 19218–19253, https://doi.org/10.1039/c5ta03471j

[42] S. Mahendrakar, M. Anna, J.S. Kumar, M.J. Reddy, Electrical and FTIR studies of plasticized polymer-salt electrolyte membrane and application to lithium ion batteries, Int J. Appl. Chem. 13 (2017) 197–210.

[43] Y. Li, H. Wang, Composite solid electrolytes with NASICON-Type LATP and PVdF–HFP for solid-state lithium batteries, Ind. Eng. Chem. Res. 60 (2021) 1494–1500, https://doi.org/10.1021/acs.iecr.0c05075

[44] M. Riley, P.S. Fedkiw, S.A. Khan, Transport properties of lithium hectorite-based composite electrolytes, pp.Article. A667, J. Electrochem Soc. 149 (2002), https://doi.org/10.1149/1.1470652

[45] J. Zhao, L. Wang, X. He, C. Wan, C. Jiang, Determination of lithium-ion transference numbers in $LiPF_6$–PC solutions based on electrochemical polarization and NMR measurements, pp.Article.A292, J. Electrochem Soc. 155 (2008), https://doi.org/10.1149/1.2837832

[46] T. Wei, Z.H. Zhang, Z.M. Wang, Q. Zhang, Y.S. Ye, J.H. Lu, Z.U. Rahman, Z.W. Zhang, PVDF-HFP / LiTFSI / Succinonitrile for High-Performance Solid-State Lithium Metal Batteries, ACS Appl. Energy Mater. 3 (2020) 9428–9435, https://doi.org/10.1021/acsaem.0c01872

[47] S.A. Suthanthiraraj, M.K. Vadivel, Effect of propylene carbonate as a plasticizer on $(PEO)_{50}AgCF_3SO_3$:SnO_2 nanocomposite polymer electrolyte, Appl. Nanosci. 2 (2012) 239–246, https://doi.org/10.1007/s13204-012-0099-3

[48] L.Z. Fan, J. Maier, Composite effects in poly(ethylene oxide)-succinonitrile based all-solid electrolytes, Electrochem Commun. 8 (2006) 1753–1756, https://doi.org/10.1016/j.elecom.2006.08.017

[49] W. Zhang, J. Nie, F. Li, Z.L. Wang, C. Sun, A durable and safe solid-state lithium battery with a hybrid electrolyte membrane, Nano Energy 45 (2018) 413–419, https://doi.org/10.1016/j.nanoen.2018.01.028

[50] J. Jie, Y. Liu, L. Cong, B. Zhang, W. Lu, J. Zhang, H. Liu, L. Xie, Sun, High-performance PVDF-HFP based gel polymer electrolyte with a safe solvent in Li metal polymer battery, J. Energy Chem. 48 (2020) 80–88, https://doi.org/10.1016/j.jechem.2020.01.019

[51] J. Huang, Y. Huang, Z. Zhang, H. Gao, C. Li, $Li6.7La_3Zr_{1.7}Ta_{0.3}O_{12}$ Reinforced PEO/PVDF-HFP based composite solid electrolyte for all solid-state lithium metal battery, Energy Fuels 34 (2020) 15011–15018, https://doi.org/10.1021/acs.energyfuels.0c03124

[52] H. Fan, C. Yang, X. Wang, L. Liu, Z. Wu, J. Luo, R. Liu, UV-curable PVdF-HFP-based gel electrolytes with semi-interpenetrating polymer network for dendrite-free Lithium metal batteries, pp.Article.114308, J. Electro Chem. 871 (2020), https://doi.org/10.1016/j.jelechem.2020.114308

[53] H. Yang, D. Mu, B. Wu, J. Bi, L. Zhang, S. Rao, Improving cathode/$Li_{6.4}La_3Zr_{1.4}Ta_{0.6}O_{12}$ electrolyte interface with a hybrid PVDF-HFP-based buffer layer for solid lithium battery, J. Mater. Sci. 55 (2020) 11451–11461, https://doi.org/10.1007/s10853-020-04701-8

[54] S. Yi, T. Xu, L. Li, M. Gao, K. Du, H. Zhao, Y. Bai, Fast ion conductor modified double-polymer (PVDF and PEO) matrix electrolyte for solid lithium-ion batteries, pp.Article. 115419, Solid State Ion. 355 (2020), https://doi.org/10.1016/j.ssi.2020.115419

[55] J. Cheng, G. Hou, Q. Sun, Z. Liang, X. Xu, J. Guo, L. Dai, D. Li, X. Nie, Z. Zeng, P. Si, L. Ci, Cold-pressing PEO/LAGP composite electrolyte for integrated all-solid-state lithium metal battery, pp.Article. 115156, Solid State Ion. 345 (2020), https://doi.org/10.1016/j.ssi.2019.115156

[56] B.J. Bu, P. Leung, C. Huang, S.H. Lee, P.S. Grant, Co-spray printing of LiFePO4 and PEO-Li1.5Al0.5Ge1.5(PO4)3 hybrid electrodes for all-solid-state Li-ion battery applications, J. Mater. Chem. A. 7 (2019) 19094–19103, https://doi.org/10.1039/c9ta03824h

[57] X. Fu, Y. Li, C. Liao, W. Gong, M. Yang, R.K.Y. Li, S.C. Tjong, Z. Lu, Enhanced electrochemical performance of solid PEO/LiClO4 electrolytes with a 3D porous Li6.28La3Zr2Al0.24O12 network, pp.Article. 107863, Compos Sci. Technol. 184 (2019), https://doi.org/10.1016/j.compscitech.2019.107863

[58] X. Yang, X. Gao, C. Zhao, Q. Sun, Y. Zhao, K. Adair, J. Luo, X. Lin, J. Liang, H. Huang, L. Zhang, S. Lu, R. Li, X. Sun, Suppressed dendrite formation realized by selective Li deposition in all-solid-state lithium batteries, Energy Storage Mater. 27 (2020) 198–204, https://doi.org/10.1016/j.ensm.2020.01.031

[59] L. Balo, H. Gupta, S.K. Singh, V.K. Singh, A.K. Tripathi, N. Srivastava, R.K. Tiwari, R. Mishra, D. Meghnani, R.K. Singh, Development of gel polymer electrolyte

based on LiTFSI and EMIMFSI for application in rechargeable lithium metal battery with GO-LFP and NCA cathodes, J. Solid State Electrochem 23 (2019) 2507–2518, https://doi.org/10.1007/s10008-019-04321-6
[60] L. Chen, Y. Li, S.P. Li, L.Z. Fan, C.W. Nan, J.B. Goodenough, PEO/garnet composite electrolytes for solid-state lithium batteries: From "ceramic-in-polymer" to "polymer-in-ceramic, Nano Energy 46 (2018) 176–184, https://doi.org/10.1016/j.nanoen.2017.12.037
[61] D. Li, L. Chen, T. Wang, L.Z. Fan, 3D fiber-network-reinforced bicontinuous composite solid electrolyte for dendrite-free lithium metal batteries, ACS Appl Mater Interfaces (2018) 7069–7078, https://doi.org/10.1021/acsami.7b18123
[62] C.M. Julien, A. Mauger, Review of 5-V electrodes for Li-ion batteries: status and trends, Ionics 19 (2013) 951–988, https://doi.org/10.1007/s11581-013-0913-2
[63] I. Gunasekara, S. Mukerjee, E.J. Plichta, M.A. Hendrickson, K.M. Abraham, A study of the influence of lithium salt anions on oxygen reduction reactions in Li-air batteries, J. Electrochem Soc. 162 (2015) A1055–A1066, https://doi.org/10.1149/2.0841506jes
[64] D.L. Pavia, G.M. Lampman, G.S. Kriz, J.R. Vyvyan. Introduction to spectroscopy, fourth ed., Brooks/cole cemgage learning, united state of america, (2008).
[65] P.S. Kumar, A. Sakunthala, M.V. Reddy, P. Moni, Structural, morphological, electrical and electrochemical study on plasticized PVdF-HFP/PEMA blended polymer electrolyte for lithium polymer battery application, Solid State Ion. 319 (2018) 256–265, https://doi.org/10.1016/j.ssi.2018.02.022
[66] P. Viswanath, M.Yoshimura Light-induced, reversible phase transition in polyvinylidene fluoride-based nanocomposites, pp. Article.1519, SN Appl. Sci. 1 (2019), https://doi.org/10.1007/s42452-019-1564-3
[67] J. Hennessy, S. Nikzad, Atomic layer deposition of lithium fluoride optical coatings for the ultraviolet, pp.Article.46, Inorganics 6 (2018), https://doi.org/10.3390/inorganics6020046
[68] M.K. Vyas, A. chandra, Ion–electron-conducting polymer composites: promising electromagnetic interference shielding material, ACS Appl. Mater. Interfaces 8 (2016) 18450–18461.
[69] S.G.Greenbaum L.F. O'donnell, Review of multivalent metal ion transport in inorganic and solid polymer electrolytes, Batteries 7 (2021) 1–27, https://doi.org/10.3390/batteries7010003
[70] J. Liu, Z. Khanam, R. Muchakayala, S. song, Fabrication and characterization of Zn-ion-conducting solid polymer electrolyte films based on PVdF-HFP/$Zn(Tf)_2$ complex system, J. Mater. Sci.: Mater. Electron. 31 (2020) 6160–6173, https://doi.org/10.1007/s10854-020-03169-1
[71] M.Y. Zhang, M.Z. Li, Z. Chang, Y.F. Wang, J. Gao, Y.S. Zhu, Y.P. Wu, W. Huang, A sandwich PVDF/HEC/PVDF gel polymer electrolyte for lithium ion battery, Electro Acta 245 (2017) 752–759, https://doi.org/10.1016/j.electacta.2017.05.154
[72] Z. Liu, G. Li, A. Borodin, X. Liu, Y. Li, F. Endres, In situ X-ray photoelectron spectroscopy investigation of the solid electrolyte interphase in a Li/$Li_{6.4}Ga_{0.2}La_3Zr_2O_{12}$/$LiFePO_4$ all-solid-state battery, J. Solid State Electrochem. 23 (2019) 2107–2117, https://doi.org/10.1007/s10008-019-04296-4